npj computational materials

www.nature.com/npjcompumats

ARTICLE OPEN

Check for updates

Dual activation and C-C coupling on single atom catalyst for CO_2 photoreduction

Fu-li Sun[1], Cun-biao Lin[1], Wei Zhang[1], Qing Chen[2], Wen-xian Chen[1], Xiao-nian Li[1] and Gui-lin Zhuang[1]✉

An excellent single-atomic photocatalyst, Ti@C_4N_3, is theoretically found to effectively convert CO_2 to C_2H_6 by density functional theory (DFT) calculations and non-adiabatic molecular dynamics (NAMD) simulations. The Ti@C_4N_3 photocatalyst has remarkable stability both thermally, chemically, and mechanically. Electronically, it has strong absorption properties ($\lambda = 327.77$ and 529.61 nm), suitable band positions, and a long photogenerated electron lifetime ($\tau_e = 38.21$ ps), allowing photogenerated electrons to migrate to the surface. Notably, the high-valence active site effectively activates two CO_2 through dual activation: Under light irradiation, the weakly adsorbed CO_2 undergoes photo-induced activation by the photoelectron of conduction band minimum (CBM); without light, the high Lewis acidity of the Ti site induces CO_2 activation through back-donating π-bond. Contrast simulation results uncovered that dual activation of CO_2 is attributed to the thermal and photonic synergy. Furthermore, two activated CO_2 species under light easily couple to form oxalate with the barrier of 0.19 eV, and further reduced to C_2H_6 with a low activation energy of 1.09 eV.

npj Computational Materials (2023)9:220 ; https://doi.org/10.1038/s41524-023-01177-3

INTRODUCTION

The latest few years has witnessed a significant global push towards achieving carbon neutrality as a response to the escalating impact of greenhouse gases (e.g. CO_2) on the planet[1,2]. Compared to other strategies (directly reducing CO_2 emission, CO_2 capture and storage, chemical conversion of CO_2 triggered by heat or electric energy), the conversion of solar-powered CO_2 photoreduction to value-added chemicals or fuels[3,4] (e.g. CH_3OH, CH_4, C_2H_4, and C_2H_6) is an appealing and green solution to ameliorate energy shortages as well as reduce CO_2 emission. Essentially, however, activation of CO_2 is both thermodynamically and kinetically difficult because of the two delocalized π_3^4 bonds with the bond length of 1.16 Å. Thus, it is challenging to transform CO_2 selectively into other chemicals at mild reaction conditions.To this end, much effort has been made to investigate the developments of photocatalysts for CO_2 reduction reaction (CO_2RR), e.g. metal nanoparticle[5], metal oxides[6] and single site catalysts[7].

Photocatalysis is a light-driven process that uses a semiconductor catalyst to generate excited electrons and holes when exposed to photons with sufficient energy. These charge carriers trigger various redox reactions, resulting in the formation of end products. Within this context, CO_2 photoreduction involve the C_1 products[8] (e.g. CO[7], CH_3OH[9], CH_4[10]), C_2 products[11,12] (C_2H_6[13], C_2H_5OH[14], CH_3COOH[15], C_2H_4[3] and so on) and C_3 products[16] (C_3H_8[17], CH_3COCH_3[18] and so on). Compared to C_1 product, however, rational design of high-performance (e.g. high selectivity) photocatalysts for multi-carbon product is highly challenging. In this vein, single-atom catalysts (SACs)[19], featuring catalytic activity adjustability as well as designed synthesis diversity[20], shown good photocatalytic performance for CO_2RR, e.g. Er_1/CN-NT[21], Fe SAS/Tr-COF[22]. Generally, an active site on heterogeneous catalysts can activate only one CO_2, leading to C_2 coupling steps requiring the synergistic collaboration of adjacent sites. Thus, C_2 coupling step during CO_2RR process is of great difficult to trigger in catalysts with highly discrete sites (e.g. SACs) due to limited reductive electronic sources as well as high atomically dispersion of active sites[23–26].

Herein, we theoretically designed an outstanding single-atom photocatalysts Ti@C_4N_3 by a combination of DFT and NAMD simulations. The supporting Ti@C_4N_3 photocatalyst features excellent stability, good absorption properties, suitable band positions and long photocarrier lifetime. Notably, real-time time dependent DFT (rt-TDDFT) simulation reveal that high-valence Ti site renders the dual activating CO_2 on Ti@C_4N_3: high Lewis-acidity of Ti site can thermally induce activation of CO_2 by π back-donating bond without light; and under visible light irradiation the weak-adsorbed CO_2 undergoes photo-induced activation by the photoelectron from CBM. Catalytic studies reveal that the two activated CO_2 is easily coupled to be oxalate, which is further reduced to be C_2H_6.

RESULTS

Stability of Ti@C_4N_3. Via three-step strategies (binding energy, band gap and adsorption energy of CO_2), we systematically screen out Ti@C_4N_3 as a potential photocatalyst (Detailed information see Supplementary Information file). Furthermore, we conduct a comprehensive stability investigation of Ti@C_4N_3 in three aspects: thermal stability, chemical stability in aqueous liquids, and mechanical stability. Firstly, Ab-initio molecular dynamic (AIMD) simulations were firstly carried out for a duration of 10 ps at a temperature of 500 K and indicate that both the energy and bonds of the structure fluctuates within a constant range, shining light on excellent thermal stability up to 500 K (see Fig. 1a). To further identify the thermal stability of SACs, an essential factor is the potential for single-atom agglomeration on the substrate. Studying the aggregation process of Ti atoms on the C_4N_3 surface,

[1]H-PSI Computational Chemistry Lab, Institute of Industrial Catalysis, State Key Laboratory Breeding Base of Green-Chemical Synthesis Technology, College of Chemical Engineering, Zhejiang University of Technology, Hangzhou 310032, PR China. [2]Surface Lab 10, Institute of Physics, Chinese Academy of Sciences, Beijing, PR China.
✉email: glzhuang@zjut.edu.cn

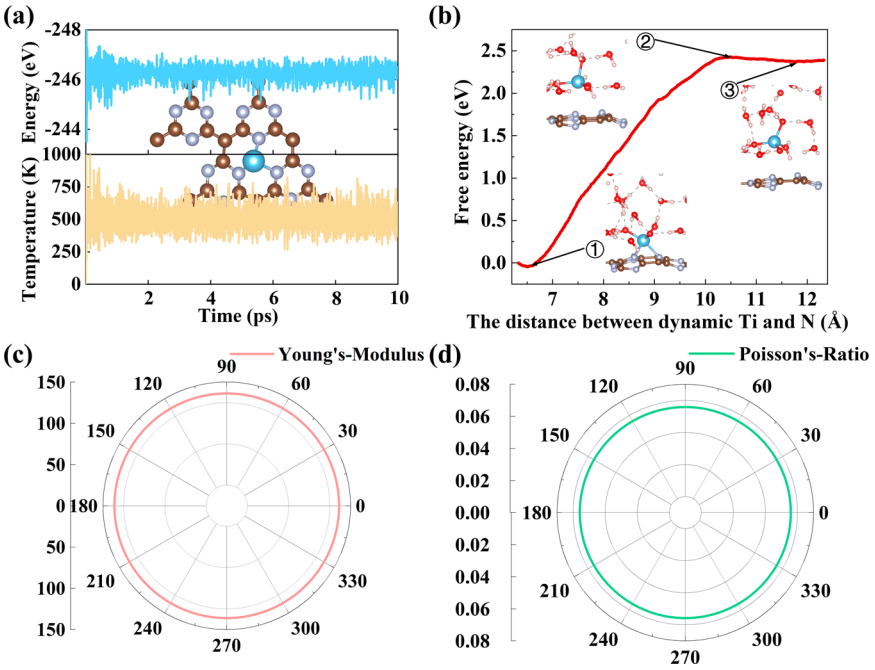

Fig. 1 Calculation of stability. a Total energy fluctuation of Ti@C_4N_3 during AIMD simulation at 500 K. **b** Free energy profile during of Ti atom dissociated from C_4N_3 surface in aqueous solvent. **c**, **d** Polar diagrams of Young's modulus and Poisson's ratio of Ti@C_4N_3, respectively.

the climbing image-nudged elastic band (CI-NEB) method was employed to identify diffusion pathway and calculate diffusion barriers (see Supplementary Fig. 9). The results reveal that, when a single Ti atom aggregates with its nearest neighboring Ti atom, the first Ti atom initially diffuses from the current N_3 hollow site to a middle site between them, encountering a barrier of $E_a = 2.38$ eV. Subsequently, the other Ti atom also migrates to the vicinity of this middle site to agglomerate with the first Ti atom, forming a Ti-Ti distance of $d_{(Ti\text{-}Ti)} = 2.603$ Å, with the uphill barrier being $E_a = 3.93$ eV, which represents the rate-determining step (RDS) for aggregation. The entire process of aggregation between the two Ti atoms is endothermic, involving an enthalpy change of 4.79 eV. These results indicate that the aggregation of single Ti atoms on C_4N_3 substrate is exceptionally challenging both thermodynamically ($\Delta H = 4.79$ eV) and kinetically ($E_a = 3.93$ eV). Consequently, Ti@C_4N_3 remains thermodynamically robust under photocatalytic conditions. To gauge chemical stability on aqua liquid environment, a solid−liquid interface model is constructed in Supplementary Fig. 10. The equilibrium structure was used to calculate the kinetic activation energy of Ti atom leaching from N_3C site. The "slow-growth" method[27] involves selecting the reaction coordinate in which the Ti-N bonds are elongated (see Fig. 1b). The analysis reveals that the free energy progressively increases with the displacement of the Ti atom from the surface, culminating in a value of 2.47 eV at the reaction endpoint, shedding light on the extreme difficulty of the three Ti−N bonds breaking under aqua environment[28]. Next, mechanical stability are performed by calculating the independent elastic stiffness tensor components. For this two-dimensional (2D) lattice with tetragonal symmetry, the independent elastic constants are $C_{11} = C_{22} = 136.08$ GPa and $C_{12} = 8.96$ GPa, fully meeting the Born−Huang criteria ($C_{11} > 0$ and $C_{11} > |C_{12}|$)[29]. Moreover, Ti@C_4N_3 feature the smaller Young's modulus of 136.25 GPa than those of many other 2D materials (1000 GPa for graphene[30], 330 GPa for MoS_2[31] and 279 GPa for h-BN[32]). Meanwhile, the Poisson's ratio (0.066) of Ti@C_4N_3 reflects its isotropically higher stiffness than that of Zn metal (0.27). Generally, Ti@C_4N_3 catalyst has excellent mechanical stability.

Optical properties and Photocarrier Dynamics of Ti@C_4N_3: Electronically, compared to the main contribution of N atoms for valance band maximum (VBM) and CBM of C_4N_3, the VBM of Ti@C_4N_3 is also concentrated on the 2*p* states of N atoms, while the CBM is accumulated at 3*d* state of Ti atom (see Fig. 2a, b). The pristine C_4N_3 features conductor property, where the 2*p* states of N atoms occupy across the Fermi level, while for Ti@C_4N_3 the 3*d* state of Ti atom occupy the Fermi level above instead of 2*p* states in N atoms and effectively reduce band dispersion at the vicinity of Fermi level, rendering to open band gap of Ti@C_4N_3 (see Fig. 2c). It can be seen from the band gap that Ti@C_4N_3 ($E_g = 0.97$ eV) from HSE-06 calculations has two distinct absorption peaks (327.77 and 529.61 nm) show in Fig. 2d, which are redshifted by 52.37 and 254.21 nm compared to the maximum absorption peak of pristine C_4N_3 ($\lambda = 275.40$ nm). Therefore, the Ti atoms loading enables the enhancement of C_4N_3 in the absorption of visible light, fully improving the ability to capture sunlight.

Furthermore, the temperature dependence of the optical properties of Ti@C_4N_3 was investigated. According to the electron-phonon interaction[33], we utilize one-shot method to sample the cartesian coordinates of atoms at different temperatures[34–36], and finally obtain the average values of samples at different coordinate sets at a given temperature ranging from 273.15 K to 373.15 K with the step size of 10 K. The band gap (see Supplementary Fig. 11a) of Ti@C_4N_3 calculated by the GW method[37] indicated that the band gap decreases with the increase of temperature, compatible with most of semiconductors. In addition, the temperature does not have a notable impact on the probability of electron transition from VBM to CBM (see Supplementary Fig. 11b), as evidenced by the variation trend in sum result of the squares of the dipole transition matrix elements (P^2) at different *k* points. Furthermore, the effect of electron-phonon interaction on carrier mobility was indirectly assessed by the effective mass of the carriers (see Supplementary Fig. 11c, d). Photogenerated electron effective mass is temperature-insensitive with around $4m_o$, whereas photogenerated hole effective mass decreases with temperature. The effective masses of photogenerated electrons and holes tend to approach each other with increasing temperature, resulting in faster carrier recombination

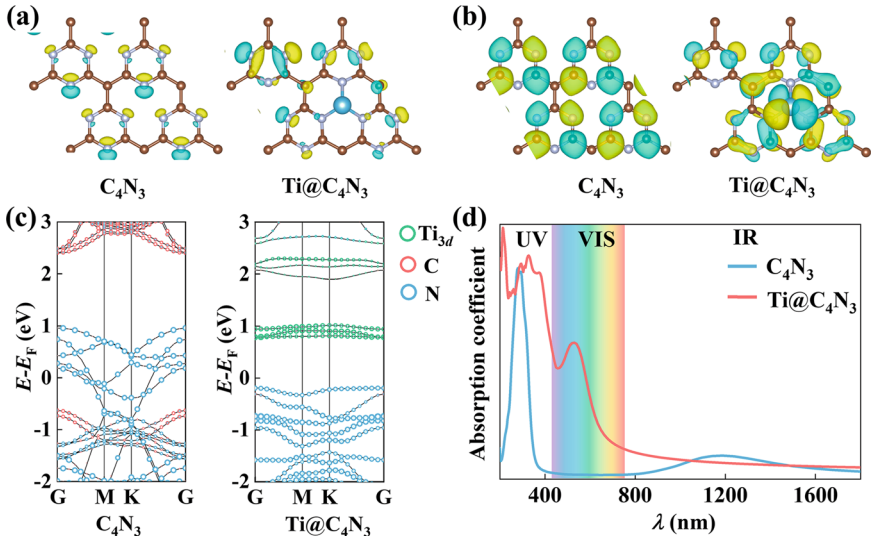

Fig. 2 Optical properties. a VBM and **b** CBM distributions of C_4N_3 and Ti@C_4N_3, respectively. **c** Distribution of C, N and Ti atoms on the energy band structure of C_4N_3 and Ti@C_4N_3 respectively. The coordinates of the highly symmetric points are as follows: G (0.00 0.00 0.00), M (0.50 0.00 0.00), K (0.33 0.33 0.33). **d** Optical adsorption spectra of pristine C_4N_3 and Ti@C_4N_3, their absorption coefficients are illustrated by blue and pink lines, respectively.

during transport and contributing to the low quantum efficiency commonly observed in semiconductor photocatalytic materials. Essentially, non-radiative relaxation and molecular thermal vibrations in semiconductors can lead to photothermal effects, which can reduce the apparent activation energy of photocatalysis and promote carrier mobility or reactant mass transfer. However, excessive temperature can lead to a stronger photothermal effect, causing the effective mass of photogenerated electrons to exceed that of holes, which can further accelerate carrier recombination and reduce photocatalytic activity. Thus, the lower m_e^* than m_h^* demonstrated Ti@C_4N_3 keeps high photocatalytic activity up to 373 K.

The dynamics of photogenerated carriers is an important factor affecting the quantum efficiency of photocatalytic reaction. Ab-initio NAMD simulations show that after light excitation the photogenerated electrons accumulate on the CBM of Ti@C_4N_3, due to the separation of photogenerated carriers. By fitting the long-time evolution curve with $P(t) = exp(-t/\tau)$[38] (see Supplementary Fig. 12), the lifetime (τ_e) of the photogenerated electron is 38.21 ps. The picosecond-range lifetime of photogenerated electrons in Ti@C_4N_3 semiconductor suggests that they have ample time to migrate to the catalyst surface and engage in the reduction reaction. These results demonstrated that the generation of Ti@C_4N_3 photogenerated carriers is very fast (femtosecond magnitude), much higher than the carrier trapping and compounding (picosecond magnitude), which is consistent with the characteristic time of photocatalysts reported in other literatures[39,40]. Thus, ensuring enough photogenerated carriers to migrate to the surface and undergo surface charge transfer for the photocatalytic reaction. To sum up, Ti@C_4N_3 photocatalyst has excellent photocatalytic activity.

Activation Mechanism of CO_2. As a crucial prerequisite for catalytic reaction, the reactant adsorption properties were of great importance for the activation[41]. In general, the adsorption strength is associated with activation degree of reactant. The CO_2 molecule, featuring linear configuration with two π_3^4 bonds, possesses the non-bonding highest occupied molecular orbital (HOMO) with energy level −10.36 eV and the σ-type and π-type antibonding lowest unoccupied molecular orbital (LUMO) with energy level of 0.36 eV and 0.65 eV respectively (see Supplementary Fig. 15). Activating CO_2 poses a challenge as transferring electrons from the deep-energy level HOMO to the active site of the catalyst incurs a significant energetic penalty. Conversely, the active site of the catalyst donates electrons to the LUMO of CO_2 to facilitate the activation process.

The AIMD simulation results provide insight into the activation process of CO_2 by Ti@C_4N_3. When CO_2 approaches the catalyst, its bond angle decreases from 180° to about 135° within 30 fs, and the two C-O bond lengths gradually elongate from 1.16 Å to 1.30 Å and 1.20 Å, respectively (see Supplementary Fig. 16a, b). The chemisorption characteristic is revealed by the obtained adsorption energy of −1.05 eV, indicating complete activation of the CO_2 molecule both energetically and structurally through thermal-induced activation. Bader charge analysis indicates that the catalyst donates 0.65 |e| electrons to the adsorbed CO_2 by back donating π bond (see Fig. 3a). The energy levels of Ti *d* orbitals and CO_2 π^* orbitals are matched, leading to partial occupation of the formed *d*-π^* orbitals and spin-polarization near the Fermi level. This results in a 0.2 eV energy level reduction in spin-up *d*-π^* states compared to spin-down *d*-π^* states (see Supplementary Fig. 17a). The well-dispersed π^* states of CO_2 below the Fermi level also validate activation states. Despite the adsorption of CO_2, the Ti site retains a charge of 2.31 |e| due to the high valence of Ti (IV) ions.

In photocatalytic reactions, the gas hourly space velocity (GHSV) of CO_2 is typically high, which increases the probability of multiple collisions between the substrate and catalyst. Therefore, it is necessary to investigate the multiple adsorptions of CO_2 on the catalyst. The AIMD simulation results of dual CO_2 adsorption on Ti@C_4N_3 indicate that after 10 ps, the first adsorbed CO_2 (CO_2-1) still features structural bending of about 45° and bond-length stretching of about 0.13 Å (see Supplementary Fig. 19a, b). However, the second CO_2 (CO_2-2) molecule maintains a linear configuration with weak physisorption of −0.39 eV adsorption energy. Electronically, the CO_2-2 only involves 0.03 |e| electrons from the substrate and therefore attains a non-activated state (see Fig. 3b). Supplementary Fig. 17b shows that the Ti *d* orbitals can only partially match the π^* orbitals of the CO_2-2 above the Fermi level, revealing its weak adsorption on the catalyst. In summary, for high GHSV of CO_2 gas, Ti@C_4N_3 activates only one CO_2 molecule, accompanied by weak adsorption of another CO_2 molecule.

As is well known, photocatalytic reaction proceeds under continuous light irradiation[42]. Whether it is possible for weakly adsorbed CO_2-2 molecule to be activated under light? Thus, ab initio

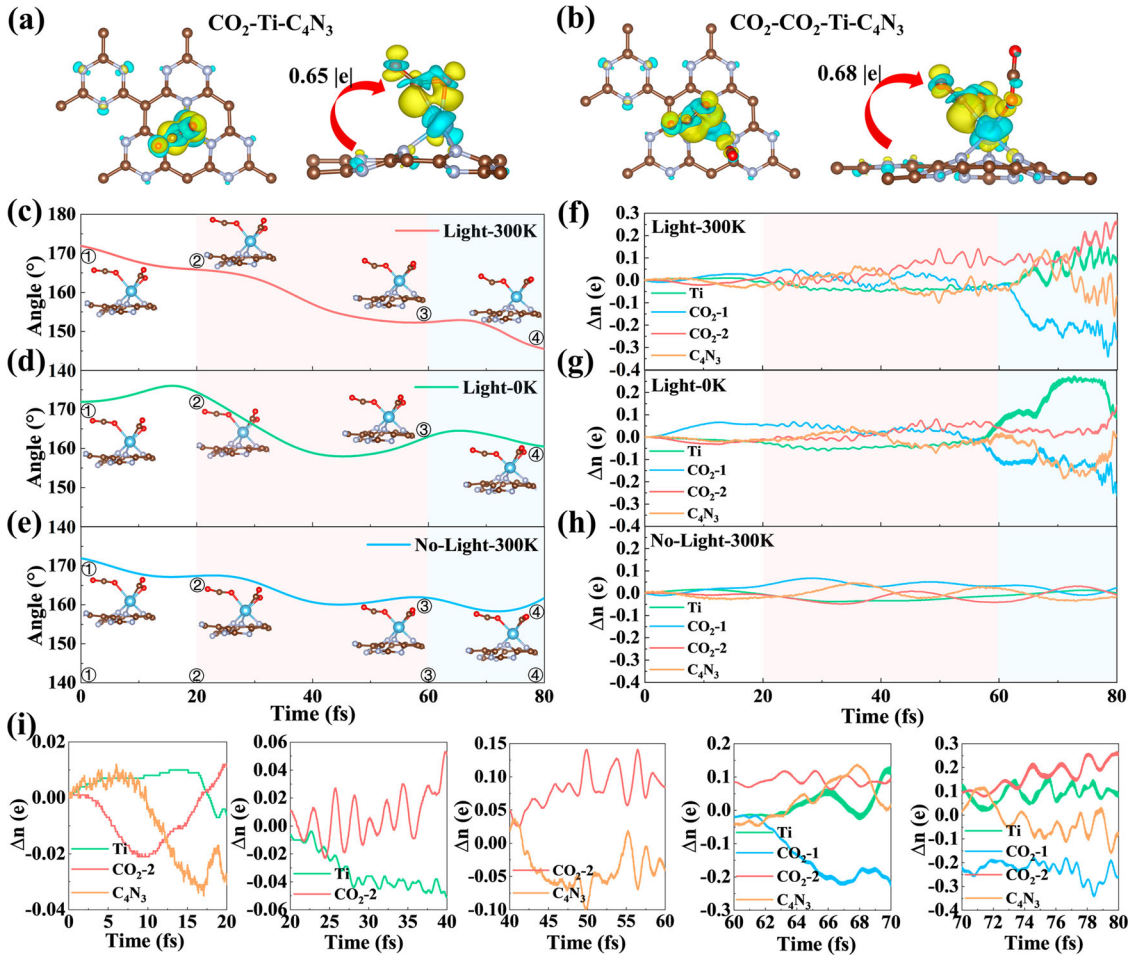

Fig. 3 Activation mechanism of CO_2 molecules. Optimised structure of CO_2 adsorption configuration, differential charge density, bader charge and the orbital interaction of CO_2 and Ti@C_4N_3, **a** the adsorption of only one CO_2 molecule, **b** the adsorption of two CO_2 molecules. The yellow and blue areas show the accumulation and depletion of charges with the isosurface of ±0.025 e $bohr^{-3}$. The bond angle of CO_2-2 molecule on Ti@C_4N_3 evolve with time at **c** light-300K, **d** light-0K and **e** no-light-300K, respectively. Snapshots at three representative times (0, 20, 60 and 80 fs) during the CO_2-2 activation process on Ti@C_4N_3 are shown in the insets ①~④; Time evolution of electron populations for the atoms at the reaction center in the period of 0~80 fs at **f** light-300K, **g** light-0K and **h** no-light-300K, respectively; **i** Piecewise temporal evolution of electron populations at light-300K. The O atom near the Ti atom is labeled O1, and the O atom far from the Ti atom is labeled O_2.

rt-TDDFT molecular dynamics simulation under light illumination[43] (see Supplementary Fig. 22) was used to study the kinetically activation process of dual CO_2 adsorption on Ti@C_4N_3 catalyst. Fig. 3c–i depicts the dependence of geometrical factors (bond angles) and electronic populations over irradiation time. To investigate the underlying mechanism for dual activation under light, we divide the electron density into each reaction center atom by Hirshfeld charge analysis. The whole reaction process involves three distinct stages (see Fig. 3f): (1) Electron excitation (0~20 fs, white span): Under the activation of the laser pulse, C_4N_3 substrate lose about 0.03 e^- charge (at t = 17 fs). As shown in Fig. 3i, the Ti site initially acquires around 0.01 e^- charge from C_4N_3 substrate at t = 15 fs. Simultaneously, the weakly-adsorbed CO_2-2 molecule gains 0.01 e^- charge, while the Ti atom experiences a decrease of approximately 0.02 e^- from 17 fs to 20 fs. This suggests a potential charge transfer between Ti atom and CO_2-2. During this process, the bond angle of CO_2-2 becomes bent to 165° (see Fig. 3c). (2) Charge transfer (20~60 fs, pink span): In this stage, electronic populations of related species undergo significant changes compared to the first stage. Firstly, a Ti atom transfers approximately 0.05 e^- charge to a CO_2-2 molecule, causing the CO_2-2 bond angle to bend from 165° to 157° within 20~40 fs. This indicates that the singular Ti site in Ti@C_4N_3 functions as a carrier bridge, providing reductive photoelectrons to activate CO_2-2. Subsequently, C_4N_3 substrate also contributes about 0.05 e^- charge to CO_2-2 within 40~60 fs, resulting in a maximum gain of approximately 0.10 e^- charge at t = 60 fs. This reveals a charge transfer process from Ti@C_4N_3 support to CO_2-2. Concurrently, the CO_2-2 bond angle further bends from 165° to 152° at 20~60 fs, and the C-O1 bond gradually lengthens to around 1.35 Å with oscillations. This behavior indicates that the CO_2-2 molecule undergoes vibrational excitation following the charge transfer in this stage. (3) CO_2 activation deeply (60~80 fs, bule span): During the initial 10 fs (t = 60~70 fs) of this stage, the geometrical structure of CO_2-2, including bond angles and bond lengths, remains unchanged, and the electronic population of CO_2-2 shows minimal changes, displaying only slight oscillations. During this time, Ti@C_4N_3 acquires approximately 0.15 e^- charge at 67 fs. Meanwhile, thermal-activated CO_2-1 experiences a loss of approximately 0.22 e^- charge. As a result, the bond angle of CO_2-1 bends to 148° (see Supplementary Fig. 24), and the C-O bonds elongate to 1.50 and 1.40 Å, respectively (see Supplementary Fig. 23a). These changes indicate that CO_2-1 further amplifies the activation process by providing electronic feedback to Ti@C_4N_3. Furthermore, at t = 70~80 fs the CO_2-2 acquired another 0.15 e^- charge, resulting in the bond angle bending from 152° to 145° and the bond length of C-O elongating to 1.37 Å. Throughout this process, both Ti@C_4N_3 and CO_2-1 experience a reduction in their charges. Hence, the substantial activation of CO_2-2 can be attributed to the electron

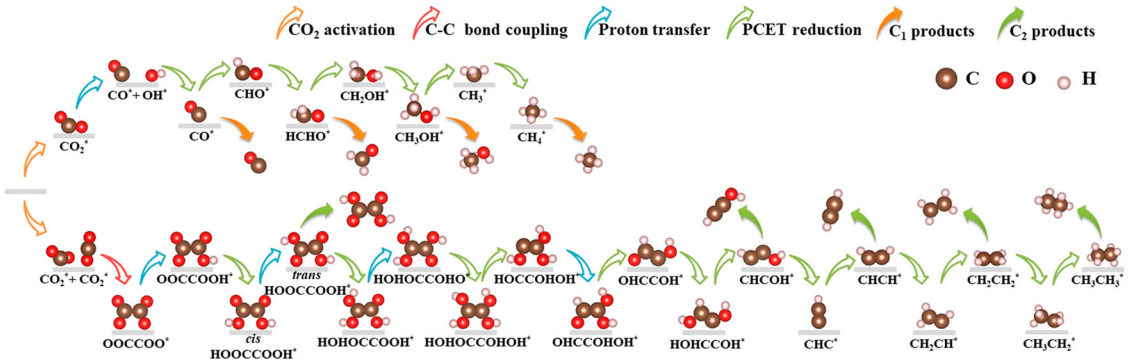

Fig. 4 Reaction pathways. Schematic illustration of the possible reaction pathways for CO_2RR on Ti@C_4N_3.

transfer from both CO_2-1 and Ti@C_4N_3 to CO_2-2, leading to strengthened interaction between the two CO_2 molecules and enabling CO_2 coupling. Furthermore, the attached simulation video (see Supplementary Video) visually illustrates the dynamic processes of CO_2 activation. This provides evidence that the Ti@C_4N_3 photocatalyst can potentially activate two CO_2 molecules simultaneously when exposed to light.

To examine thermal effects in the photocatalytic reaction, we conducted additional simulations in two conditions: (1) with light and at 0 K (light-0K); (2) without light at 300 K (no-light-300K), alongside the previously mentioned conditions under light and 300 K (light-300K). Compared to that under light-300K, the light-0K simulation features different results (see Fig. 3g). In 0~20 fs, C_4N_3 substrate has almost no electron transfer to Ti atom, Ti transfers about 0.02 e^- charge to CO_2-2 in 20~40 fs, CO_2-2 acquires the electron around 0.04 e^- charge from C_4N_3 substrate at 40~60 fs. At this point CO_2-2 gradually begins to activate and bends to approximately 160°. At 66~70 fs, C_4N_3 substrate begins to transfer some electrons to Ti atom (about 0.15 e^- charge). Subsequently, Ti provides charge to CO_2-2 around 0.13 e^- charge during 70~80 fs (see Supplementary Fig. 25). The bond length of CO_2-2 during this whole process fluctuated around 1.25 and 1.30 Å (see Supplementary Fig. 23b), respectively, and the maximum curvature was 158° at t = 45 fs, after which it fluctuated in the range of 160°. Thus, the slower electron-transfer rate at light-0K makes the activation of CO_2-2 worse than at light-300K. Under the no-light-300K, the electron densities of CO_2 and Ti@C_4N_3 do not change significantly, fluctuating roughly around 0 e^- charge because the transitions between vibrational levels are insufficient to induce electron transfers. Structurally, there were minimal changes in both the bond angle and bond length of CO_2-2. Consequently, activating two CO_2 molecules under the no-light-300K condition proved to be highly challenging. The combined results from light-300K, light-0K, and no-light-300K simulations reveal that concurrent activation of two CO_2 molecules occurs. Under light-300K, CO_2-2 undergoes significant charge transfer and structural changes compared to the no-light-300K condition, whereas it maintains an approximately linear structure under no light. Comparing light-300K and light-0K, both conditions can activate two CO_2 molecules simultaneously, but charge transfer is slow pronounced under light-0K, and the catalyst-CO_2-2 interaction is weaker. These findings suggest that a synergistic effect between photoexcitation and thermal effects plays a crucial role in the simultaneous activation of two CO_2 molecules. Light conditions are key to this dual activation, while thermal effects facilitate charge transfer via electron-phonon coupling, further enhancing CO_2-2 activation[15,44,45].

Mechanism of photocatalytic CO_2RR. To evaluate the catalytic mechanism of the CO_2RR on Ti@C_4N_3 catalysts, transition state calculations were performed utilizing DFT + U (U_{eff} = 3.79 eV) calculations. Both proton transfer and proton-coupled electron transfer (PCET) is utilized to describe the reduction mechanism of CO_2[24,46,47]. Several possible reaction pathways for the CO_2 reduction, including single CO_2 reduction and dual CO_2 reduction, were identified on the Ti@C_4N_3 (see Fig. 4). In the following *, E_a, E_{ads} and E_{des} denote the adsorption site, barrier energy, adsorption energy and desorption energy respectively. Firstly, the reduction mechanism of single CO_2 on Ti@C_4N_3 photocatalyst was studied. CO_2 molecule is activated on the catalyst to form a CO_2^* anionic intermediate. Via the first PCET, the adsorbed CO_2^* binds with H proton with two different pathways of $HCOO^*$ and $COOH^*$. Subsequently, the more stable $COOH^*$ intermediate experiences the C-O bond rupture with the uphill trend of 0.23 eV, resulting in the formation of CO^* and OH^* species co-binding with Ti site. Then through an energy barrier of 0.40 eV, the OH^* generates H_2O^* by the PCET process and desorbed from the catalyst, while under the larger energetic penalty of 1.51 eV, the CO^* is desorbed from the catalyst, which is the RDS for CO generation (see Fig. 5). Thus, it is accessible for subsequent hydrogenation on CO^*. The CO^* is hydrogenated to produce two possible species: COH^* and CHO^* with the associated barrier of E_a = 1.73 eV (COH^*) and E_a = 0.11 eV (CHO^*) (see Supplementary Fig. 26), implying the optimal product of CHO^* rather than COH^*. During the fourth PCET process, the CHO^* will involve these two processes: $CHO^* + H^+ + e^- \rightarrow HCHO^*$ and $CHO^* + H^+ + e^- \rightarrow CHOH^*$ (see Supplementary Fig. 27). The hydrogenation of CHO^* to $HCHO^*$ (E_a = 0.30 eV) is more favorable than that of $CHOH^*$ (E_a = 1.21 eV) from the perspective of kinetics. The larger adsorption energy (E_{ads} = −2.26 eV) of $HCHO^*$ on Ti@C_4N_3 leads to the desorption difficulty, while via the barrier of 0.70 eV the hydrogenation of $HCHO^*$ intermediate generates the CH_2OH^*, which further form CH_3OH^* product via the 6th PCET step with the barrier of 0.65 eV. Under the uphill barrier of 0.40 eV, the adsorbed CH_3OH^* enables hydrogenated (7th PCET) and dehydrated to CH_3^*, which is easily hydrogenated to CH_4 under the 8th PCET. The CH_4 is more readily desorbed (E_{des} = 0.56 eV) from the Ti@C_4N_3 catalyst surface than other C_1 products (such as CO, HCHO, CH_3OH), and $HCHO^* + H^+ + e^- \rightarrow CH_2OH^*$ is a RDS for CH_4 generation. In general, single adsorbed CO_2 molecule undergoes a series of hydrogenation steps to form C_2 intermediate species through four common coupling pathways: CO^*-CO^*, CO^*-COH^* or CHO^*, CO^*-CH_n^* (n = 1, 2, 3), and CH_n^*-CH_n^*[11,12,16]. Among the four pathways, a common feature is the formation of CO^* intermediates before C-C coupling. However, for SACs, the nearly identical charge distributions between neighbouring C_1 intermediates inevitably result in a strong dipole−dipole repulsion and thereby hinders C − C coupling. Apart from that as the discrete active sites and strong adsorption for crucial intermediates (−1.51 eV for CO^*, −2.74 eV for COH^*, −2.98 eV for CHO^*, −4.38 eV for CH^*, −3.70 eV for CH_2^* and −3.08 eV for CH_3^*), desorption and diffusion of these intermediates are too difficult to achieve C-C coupling through Langmuir–Hinshelwood (L-H) or Eley–Rideal (E-R) mechanisms. In summary, the generation of C_2 products via the four coupling pathways described earlier is particularly challenging when using Ti@C_4N_3 catalysts. Thus, the reduction of individual CO_2 molecule

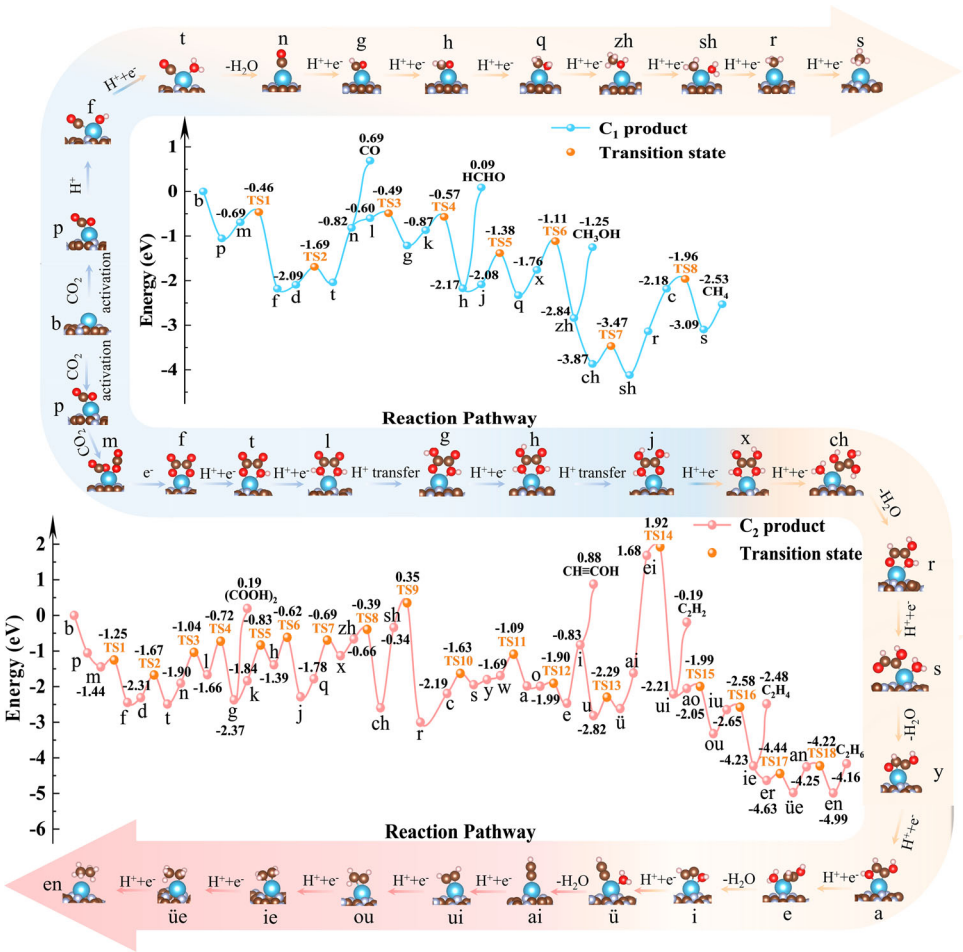

Fig. 5 CO_2RR energy barrier and reaction intermediates. Reaction mechanisms of C_1 and C_2 products. b stands for catalyst. Color codes: C, brown; N, silver; Ti, light blue; O, red; H, white.

is more inclined to generate C_1 species via the eight PCET steps, where the barriers of RDS are 1.51 eV for CO, 2.26 eV for HCHO, 1.59 eV for CH_3OH and 0.70 eV for CH_4, respectively, Thereinto, CH_4 features the highest kinetic selectivity.

Just as aforementioned, given for high GHSV of CO_2 gas, the Ti@C_4N_3 can activate two CO_2 molecules through both thermal and photonic excitation. Thus, it is whether two activated CO_2^* directly undergoes C-C coupling reaction under light irradiation. However, it is very difficult to use the ab-initio NAMD simulation to identify the whole real-time coupling process under light. Thus, we hypothesize that photon is only beneficial for the activation rather than the diffusion of intermediate. Based on CI-NEB strategy (see Supplementary Fig. 29), we found that direct coupling of two CO_2^* proceeds with the tiny barrier of 0.19 eV, which is thermodynamically easier than the coupling via previous four pathways (see Fig. 6). Such result is different from the consensus that CO^* is necessary for the formation of multicarbons (C_{2+}) products[11,48,49]. Supplementary Fig. 30 indicates that the kinetically CO_2^* to CO_2^* coupling ($E_a = 0.19$ eV) capacity is higher than that of CO_2^* to H^* proton ($E_a = 0.23$ eV). Furthermore, crystal orbital hamilton population (COHP) results in Supplementary Fig. 31 showed that negative ICOHP of C-C bond (−3.99) and Ti-O bonds (−2.82 and −2.79) sheds light on the stability of $OOCCOO^*$ on the surface of Ti@C_4N_3 catalyst and the existence of strong C-C bond[50,51]. Thus, the adsorbed $OOCCOO^*$ intermediate is able to participate in the subsequent reduction to generate multiple C_2 products (e.g. $(COOH)_2$, CH ≡ COH, C_2H_2, C_2H_4 and C_2H_6). Via the first PCET step ($OOCCOO^* + H^+ + e^- \rightarrow OOCCOOH^*$), the barrier of 0.64 eV is required for the formation of $OOCCOOH^*$, which binds with one proton to form *cis* $HOOCCOOH^*$ through the next elementary step (see Fig. 5) with the barrier of $E_a = 0.86$ eV.

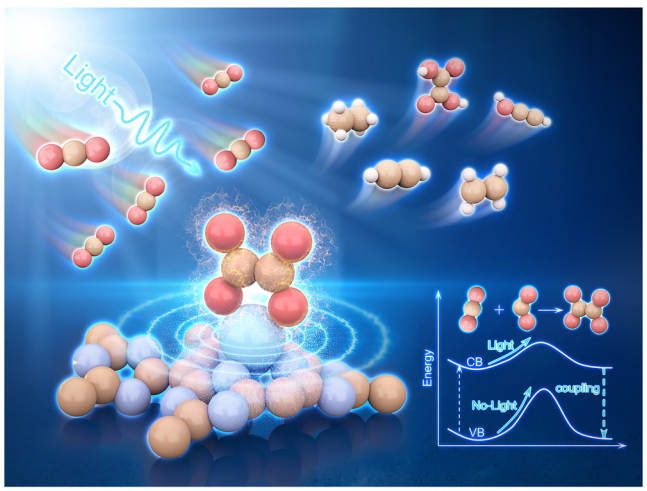

Fig. 6 Schematic diagram of two CO_2 molecules coupled. Comparison of two CO_2 coupling processes in light and no-light.

Then, via the intramolecular proton transfer, the *cis* $HOOCCOOH^*$ can undergo a structural transformation resulting in the production of *trans* $HOOCCOOH^*$ with an associated energetic penalty of 0.94 eV.

The obtained *trans* HOOCCOOH* prefers to continue hydrogenation to produce HOHOCCOOH* ($E_a = 1.01$ eV) rather than the desorption with energy of 2.56 eV. Next, HOHOCCOOH* underwent proton transfer to produce HOHOCCOHO* with the barrier of 0.77 eV. The HOHOCCOHO* generates species HOHOCCOHOH* is demands an energy barrier of 1.09 eV, which is further reduced to HOCCOHOH* by C-O bond fracture dehydration ($E_a = 0.27$ eV). Due to the structural instability of HOCCOHOH*, the proton transfer from the hydroxyl group to the C atom with the formation of carbonyl group ($E_a = 0.69$ eV), resulting in OHCCOHOH* intermediate. Subsequently, OHCCOHOH* undergoes PCET dehydration with 0.56 eV barrier to yield OHCCOH*, which must overcome a 0.60 eV barrier to undergo hydrogenation and form an O-H bond, resulting in the generation of HOHCCOH*. Rapid hydrogenation of HOHCCOH* leads to C-O bond breakage to emerge CHCOH* and H_2O ($E_a = 0.09$ eV). On Ti@C_4N_3 catalyst, the stronger adsorption of CHCOH* ($E_{ads} = -1.71$ eV) benefits further hydrogenation and dehydration to obtain CHC* through the barrier of 0.53 eV. The successive hydrogenation of CHC* → CHCH* → CH_2CH^* → $CH_2CH_2^*$ → $CH_3CH_2^*$ → $CH_3CH_3^*$occurs under the barriers of 0.24, 0.06, 0.07, 0.19 and 0.03 eV, respectively. Despite the formation of C_2H_2 and C_2H_4 products, the subsequent hydrogenation process leads to the final production of C_2H_6 due to their adsorption energy ($E_{ads} = 2.02$ eV for C_2H_2, 1.75 eV for C_2H_4) compared to the hydrogenation barrier. Generally, during the coupled hydrogenation of two CO_2 on Ti@C_4N_3, various products are formed with different energy barriers of 2.56 eV for $(COOH)_2$, 1.71 eV for CH ≡ COH, 2.02 eV for C_2H_2, 1.75 eV for C_2H_4 and 1.09 eV for C_2H_6, respectively. Therefore, C_2H_6 is determined to be the optimal product via fourteen-electron reduction, and the generation of the HOHOCCOHOH* intermediate is the RDS for the entire reaction in both kinetics ($E_a = 1.09$ eV) and thermodynamics ($\Delta G_{max} = 1.57$ eV).

DISCUSSION

In summary, by utilizing DFT calculation and ab-initio NAMD simulation, we build the computational frameworks to screen an outstanding single-atom photocatalysts Ti-supported 2D C_4N_3 material, Ti@C_4N_3. Structurally, the Ti@C_4N_3 catalyst shown the excellent stabilities both thermally, chemically and mechanically. Electronically, such catalyst has great potential as a photocatalyst for CO_2 reduction: two main absorption peaks (327.77 and 529.61 nm), suitable band positions (0.002 eV for VBM and −0.968 eV for CBM) and long photocarrier lifetime (38.21 ps for electron), ensuring that enough photogenerated electrons migrate to the surface and participate in photocatalytic CO_2RR. Essentially, such properties are intimately tied with the doping Ti atom, embodying the fundamental transformations from conductor to semiconductor. Interestingly, under the high GHSV of CO_2, such high-valence of doping Ti ion renders the dual activation of CO_2: Without light, high Lewis-acidity of Ti site thermally induces activation of CO_2 by back-donating π-bond; and under visible light irradiation another weak-adsorbed CO_2 attains the photoelectron from Ti site through CBM and thereby undergoes photo-induced activation. Catalytic mechanism studies systematically reveal that with the barrier of 0.19 eV the two activated CO_2 is easily coupled to be oxalate, which is further reduced to be C_2H_6 ($E_a = 1.09$ eV). Our finding reveals the possibility of dual activations (thermally induced activation and photo-induced activation) during the photocatalytic CO_2 reductions.

METHODS

Ground-State Calculations. DFT calculations (geometrical optimization, electronic properties and catalytic mechanism) were carried out by VASP package[52] (6.3.1) using Perdew−Burke−Ernzerhof[53] (PBE) functional and projector-augmented wave[54] (PAW) pseudopotential. Detailed computational information was presented in Supplementary Data file.

Excited-state Dynamic calculations. The photocarrier dynamics was simulated by using the ab initio NAMD program (Hefei-NAMD)[55]. Dual activation of CO_2 under light irradiation was identified by rt-TDDFT MD simulation utilizing the TDAP program[56]. Detailed computational information was presented in Supplementary Data file.

DATA AVAILABILITY

The computational results, including structure files, transition state calculations, excited state calculations and so on, can be found at https://archive.materialscloud.org/record/2023.178. Additional supporting data for this study is available in the article, its supplementary information files, or upon reasonable request from the corresponding authors.

CODE AVAILABILITY

VASP 6.3.1 software was obtained through commercial purchase (https://www.vasp.at/). Two open-source software (TDAP software and Hefei-NAMD software) can be obtained from http://tdap.iphy.ac.cn/ and https://github.com/QijingZheng/Hefei-NAMD, respectively.

Received: 15 June 2023; Accepted: 28 November 2023;
Published online: 11 December 2023

REFERENCES

1. Ding, M., Flaig, R. W., Jiang, H.-L. & Yaghi, O. M. Carbon capture and conversion using metal–organic frameworks and MOF-based materials. *Chem. Soc. Rev.* **48**, 2783–2828 (2019).
2. Chu, S., Cui, Y. & Liu, N. The path towards sustainable energy. *Nat. Mater.* **16**, 16–22 (2017).
3. Gao, W. et al. Vacancy-defect modulated pathway of photoreduction of CO_2 on single atomically thin $AgInP_2S_6$ sheets into olefiant gas. *Nat. Commun.* **12**, 4747 (2021).
4. Rao, H., Schmidt, L. C., Bonin, J. & Robert, M. Visible-light-driven methane formation from CO_2 with a molecular iron catalyst. *Nature* **548**, 74–77 (2017).
5. Shangguan, W. et al. Molecular-level insight into photocatalytic CO_2 reduction with H2O over Au nanoparticles by interband transitions. *Nat. Commun.* **13**, 3894 (2022).
6. Huang, H. et al. Triphase Photocatalytic CO_2 Reduction over Silver-Decorated Titanium Oxide at a Gas–Water Boundary. *Angew. Chem. Int. Ed.* **61**, e202200802 (2022).
7. Ding, C. et al. Interlayer Spacing Regulation by Single-Atom Indiumδ^+–N_4 on Carbon Nitride for Boosting CO_2/CO Photo-Conversion. *Adv. Funct. Mater.* **n/a**, 2302824 (2023).
8. Li, K., Peng, B. & Peng, T. Recent Advances in Heterogeneous Photocatalytic CO_2 Conversion to Solar Fuels. *ACS Catal.* **6**, 7485–7527 (2016).
9. Ma, M. et al. Ultrahigh surface density of Co-N_2C single-atom-sites for boosting photocatalytic CO_2 reduction to methanol. *Appl. Catal. B: Environ.* **300**, 120695 (2022).
10. Liu, Q. et al. High-Yield Synthesis of Ultralong and Ultrathin Zn_2GeO_4 Nanoribbons toward Improved Photocatalytic Reduction of CO_2 into Renewable Hydrocarbon Fuel. *J.e. Am. Chem. Soc.* **132**, 14385–14387 (2010).
11. Kim, Y. et al. Time-resolved observation of C–C coupling intermediates on Cu electrodes for selective electrochemical CO_2 reduction. *Energy &. Environ. Sci.* **13**, 4301–4311 (2020).
12. Albero, J., Peng, Y. & García, H. Photocatalytic CO_2 Reduction to C_{2+} Products. *ACS Catal.* **10**, 5734–5749 (2020).
13. Wang, G., Chen, Z., Wang, T., Wang, D. & Mao, J. P and Cu Dual Sites on Graphitic Carbon Nitride for Photocatalytic CO_2 Reduction to Hydrocarbon Fuels with High C_2H_6 Evolution. *Angew. Chem. Int. Ed.* **61**, e202210789 (2022).
14. Das, K. et al. Intrinsic Charge Polarization in $Bi_{19}S_{27}Cl_3$ Nanorods Promotes Selective C-C Coupling Reaction during Photoreduction of CO_2 to Ethanol. *Adv. Mater.* **35**, 2205994 (2023).
15. Zhu, J. et al. Asymmetric Triple-Atom Sites Confined in Ternary Oxide Enabling Selective CO_2 Photothermal Reduction to Acetate. *J. Am. Chem. Soc.*, **143**, 18233–18241 (2021).
16. Pan, F. et al. Carbon Catalysts for Electrochemical CO_2 Reduction toward Multicarbon Products. *Adv. Energy Mater.* **12**, 2200586 (2022).
17. Shen, Y. et al. Room-temperature photosynthesis of propane from CO_2 with Cu single atoms on vacancy-rich TiO_2. *Nat. Commun.* **14**, 1117 (2023).

18. Zhao, K. et al. Selective electroreduction of CO_2 to acetone by single copper atoms anchored on N-doped porous carbon. *Nat. Commun.* **11**, 2455 (2020).
19. Wang, A., Li, J. & Zhang, T. Heterogeneous single-atom catalysis. *Nat. Rev. Chem.* **2**, 65–81 (2018).
20. Hai, X. et al. Scalable two-step annealing method for preparing ultra-high-density single-atom catalyst libraries. *Nat. Nanotechnol.* **17**, 174–181 (2022).
21. Ji, S. et al. Rare-Earth Single Erbium Atoms for Enhanced Photocatalytic CO_2 Reduction. *Angew. Chem. Int. Ed.* **59**, 10651–10657 (2020).
22. Ran, L. et al. Engineering Single-Atom Active Sites on Covalent Organic Frameworks for Boosting CO_2 Photoreduction. *J. Am. Chem. Soc.* **144**, 17097–17109 (2022).
23. Liu, Y., Chen, S., Quan, X. & Yu, H. Efficient Electrochemical Reduction of Carbon Dioxide to Acetate on Nitrogen-Doped Nanodiamond. *J. Am. Chem. Soc.* **137**, 11631–11636 (2015).
24. Zhao, K. & Quan, X. Carbon-Based Materials for Electrochemical Reduction of CO_2 to C_{2+} Oxygenates: Recent Progress and Remaining Challenges. *ACS Catal.* **11**, 2076–2097 (2021).
25. Thompson, M. C., Ramsay, J. & Weber, J. M. Solvent-Driven Reductive Activation of CO_2 by Bismuth: Switching from Metalloformate Complexes to Oxalate Products. *Angew. Chem. Int. Ed.* **55**, 15171–15174 (2016).
26. Dong, X., Wang, L., Wang, G. & Zhou, M. Carbon Dioxide Activation by Alkaline-Earth Metals: Formation and Spectroscopic Characterization of $OCMCO_3$ and MC_2O_4 (M = Ca, Sr, Ba) in Solid Neon. *J. Phys. Chem. A* **126**, 4598–4607 (2022).
27. Woo, T. K., Margl, P. M., Blöchl, P. E. & Ziegler, T. A Combined Car−Parrinello QM/MM Implementation for ab Initio Molecular Dynamics Simulations of Extended Systems: Application to Transition Metal Catalysis. *J. Phys. Chem. B* **101**, 7877–7880 (1997).
28. Bai, X. et al. Dynamic Stability of Copper Single-Atom Catalysts under Working. *Cond. J. Am. Chem. Soc.,* **144**, 17140–17148 (2022).
29. Wallace, D. C. Lattice Dynamics and Elasticity of Stressed Crystals. *Rev. Mod. Phys.* **37**, 57–67 (1965).
30. Lee, C., Wei, X., Kysar, J. W. & Hone, J. Measurement of the Elastic Properties and Intrinsic Strength of Monolayer Graphene. *Science* **321**, 385–388 (2008).
31. Castellanos-Gomez, A. et al. Elastic Properties of Freely Suspended MoS_2 Nanosheets. *Adv. Mater.* **24**, 772–775 (2012).
32. Peng, Q., Ji, W. & De, S. Mechanical properties of the hexagonal boron nitride monolayer: Ab initio study. *Comput. Mater. Sci.* **56**, 11–17 (2012).
33. Zhu, Z., Yao, X., Zhao, S., Lin, X. & Li, W. Giant Modulation of the Electron Mobility in Semiconductor Bi_2O_2Se via Incipient Ferroelectric Phase Transition. *J. Am. Chem. Soc.* **144**, 4541–4549 (2022).
34. Karsai, F., Engel, M., Flage-Larsen, E. & Kresse, G. Electron–phonon coupling in semiconductors within the GW approximation. *N. J. Phys.* **20**, 123008 (2018).
35. Zacharias, M. & Giustino, F. One-shot calculation of temperature-dependent optical spectra and phonon-induced band-gap renormalization. *Phys. Rev. B* **94**, 075125 (2016).
36. Bloch, F. Zur Theorie des Austauschproblems und der Remanenzerscheinung der Ferromagnetika. *Z. f.ür. Phys.* **74**, 295–335 (1932).
37. Shishkin, M. & Kresse, G. Implementation and performance of the frequency-dependent GW method within the PAW framework. *Phys. Rev. B* **74**, 035101 (2006).
38. Shi, A. et al. Direct Z-Scheme Photocatalytic System: Insights into the Formative Factors of Photogenerated Carriers Transfer Channel from Ultrafast Dynamics. *ACS Catal.* **12**, 9570–9578 (2022).
39. Ye, C., Zhang, N., Wang, D. & Li, Y. Single atomic site catalysts: synthesis, characterization, and applications. *Chem. Commun.* **56**, 7687–7697 (2020).
40. Zeng, L. et al. Photoactivation of Cu Centers in Metal–Organic Frameworks for Selective CO_2 Conversion. *Ethanol. J. Am. Chem. Soc.,* **142**, 75–79 (2020).
41. Shi, X. et al. Highly Selective Photocatalytic CO_2 Methanation with Water Vapor on Single-Atom Platinum-Decorated Defective Carbon Nitride. *Angew. Chem. Int. Ed.* **61**, e202203063 (2022).
42. Ojanperä, A., Havu, V., Lehtovaara, L. & Puska, M. Nonadiabatic Ehrenfest molecular dynamics within the projector augmented-wave method. *J. Chem. Phys.* **136**, 144103 (2012).
43. You, P. et al. Nonadiabatic Dynamics of Photocatalytic Water Splitting on A Polymeric Semiconductor. *Nano Lett.* **21**, 6449–6455 (2021).
44. Tóth, A., Bánsági, T. & Solymosi, F. Effects of H_2O on the thermal and photocatalytic reactions of ethane on supported Au. *Mol. Catal.* **440**, 19–24 (2017).
45. Wang, Z. et al. On the Mechanism of Methyl Formate Production Initiated by Photooxidation of Methanol on Rutile TiO_2(110) and TiO_2(011)-(2 × 1) Surfaces. *J. Phys. Chem. C.* **123**, 31073–31081 (2019).
46. Mayer, J. M. Bonds over Electrons: Proton Coupled Electron Transfer at Solid–Solution. *Interfaces J. Am. Chem. Soc.* **145**, 7050–7064 (2023).
47. Bard, A. J. Inner-Sphere Heterogeneous Electrode Reactions. Electrocatalysis and Photocatalysis: The Challenge. *J. Am. Chem. Soc.* **132**, 7559–7567 (2010).
48. Pérez-Gallent, E., Figueiredo, M. C., Calle-Vallejo, F. & Koper, M. T. M. Spectroscopic Observation of a Hydrogenated CO Dimer Intermediate During CO Reduction on Cu(100) Electrodes. *Angew. Chem. Int. Ed.* **56**, 3621–3624 (2017).
49. Wuttig, A., Ryu, J. & Surendranath, Y. Electrolyte Competition Controls Surface Binding of CO Intermediates to CO_2 Reduction Catalysts. *J. Phys. Chem. C.* **125**, 17042–17050 (2021).
50. Guo, X. et al. Tackling the Activity and Selectivity Challenges of Electrocatalysts toward the Nitrogen Reduction Reaction via Atomically Dispersed Biatom. *Catalysts. J. Am. Chem. Soc.* **142**, 5709–5721 (2020).
51. Deng, T. et al. Atom-Pair Catalysts Supported by N-Doped Graphene for the Nitrogen Reduction Reaction: *d*-Band Center-Based Descriptor. *J. Phys. Chem. Lett.* **11**, 6320–6329 (2020).
52. Kresse, G. & Furthmüller, J. Efficiency of ab-initio total energy calculations for metals and semiconductors using a plane-wave basis set. *Comput. Mater. Sci.* **6**, 15–50 (1996).
53. Perdew, J. P. et al. Restoring the Density-Gradient Expansion for Exchange in Solids and Surfaces. *Phys. Rev. Lett.* **100**, 136406 (2008).
54. Kresse, G. & Joubert, D. From ultrasoft pseudopotentials to the projector augmented-wave method. *Phys. Rev. B* **59**, 1758–1775 (1999).
55. Craig, C. F., Duncan, W. R. & Prezhdo, O. V. Trajectory Surface Hopping in the Time-Dependent Kohn-Sham Approach for Electron-Nuclear Dynamics. *Phys. Rev. Lett.* **95**, 163001 (2005).
56. Ma, W. et al. Recent progresses in real-time local-basis implementation of time dependent density functional theory for electron–nucleus dynamics. *Comput. Mater. Sci.* **112**, 478–486 (2016).

ACKNOWLEDGEMENTS

This work was supported by the National Natural Science Foundation of China (Grant No: 22022108, 22072135, 21671172), Zhejiang Provincial Natural Science Foundation of China (Grant No: LTGY23B010001), Natural Science Foundation of Shandong Province (ZR2020ZD35).

AUTHOR CONTRIBUTIONS

F.L.S. and G.L.Z. conceived and designed the whole study; C.B.L. performed carrier dynamic calculation; Q.C. provide PBE + *U* based TDAP software and discuss with corresponding calculations; W.Z., W.X.C. and X.N.L. discussed dual activation of CO_2 and analyze CO_2 coupling mechanism.

COMPETING INTERESTS

The authors declare no competing interests.

ADDITIONAL INFORMATION

Supplementary information The online version contains supplementary material available at https://doi.org/10.1038/s41524-023-01177-3.

Correspondence and requests for materials should be addressed to Gui-lin Zhuang.

Reprints and permission information is available at http://www.nature.com/reprints

Publisher's note Springer Nature remains neutral with regard to jurisdictional claims in published maps and institutional affiliations.